

# Imaging space weather over Europe

Jeffrey Baumgardner,<sup>1</sup> Joei Wroten,<sup>1</sup> Michael Mendillo,<sup>1</sup> Carlos Martinis,<sup>1</sup>  
 Cesare Barbieri,<sup>2</sup> Gabriele Umbriaco,<sup>2</sup> Cathryn Mitchell,<sup>3</sup> Joe Kinrade,<sup>3</sup>  
 Massimo Materassi,<sup>4</sup> Luigi Ciralo,<sup>4</sup> and Marc Hairston<sup>5</sup>

Received 6 November 2012; accepted 7 January 2013; published 25 February 2013.

[1] We describe the introduction of the first all-sky imaging system for low-light-level optical observations of the disturbed ionosphere over mid-latitude Europe. Using 6300 Å auroral emissions that come from the 200–400 km altitude range, we demonstrate that sub-visual optical patterns spanning the European continent can be obtained from a single site in Italy. Pilot observations during the 26–27 September 2011 geomagnetic storm show that the diffuse aurora’s low latitude boundary can be used to find where the poleward wall of the ionospheric trough is located. This relates directly to regions of radiowave disruptions caused by the precipitation of energetic particles from the magnetospheric plasma sheet that move to lower latitudes during space weather events. Images of stable auroral red (SAR) arcs can be used to track the magnetospheric ring current and plasmopause location, a second region of radiowave interference. Comparisons with ground-based and satellite observations of the ionosphere during the same storm demonstrate how ASI images reveal the lowest energy components of magnetospheric input to the ionosphere-thermosphere system. Such observations can be used, potentially, for both now-casting of storm effects spanning Europe, and for retrospective validation of existing models of space weather impacts at sub-auroral locations.

**Citation:** Baumgardner, J., et al. (2013), Imaging space weather over Europe, *Space Weather*, 11, 69–78, doi:10.1002/swe.20027.

## 1. Introduction

[2] Photographic recordings of the aurora were first accomplished in Europe in 1892 by Martin Brendel using exposure times that ranged from a few minutes down to several seconds [Eather, 1980]. Half a century later, the use of an “all-sky” camera to capture horizon-to-horizon views of the aurora became a central component of the International Geophysical Year of 1957–58 when 114 systems were deployed worldwide. These early systems used photographic film to record “white light” images of various auroral forms that had long fascinated visual observers. In North America, the era of all-sky photography of the aurora is mostly associated with the work of Syun Akasofu that

culminated in the unification of auroral morphologies in his classic book [Akasofu, 1968]. With the coming of image intensifier technologies, the sensitivity of detectors increased greatly and thus it became possible to record *sub-visual* emissions at specific wavelengths using narrow-band filters. The capability to image features that could not be seen with the naked eye extended the realm of solar-terrestrial physics to regions beyond the auroral oval—first poleward to document faint polar cap patches, blobs and sun-aligned arcs [Weber and Buchau, 1981; Weber et al., 1984], and then equatorward to record images of stable-auroral red (SAR) arcs [Mendillo et al., 1987; Foster et al., 1994].

[3] The SAR arc phenomenon was first discovered in Europe by Barbier [1958, 1960] using a photometer at the Haute Provence observatory in France. A review of these and other pioneering studies of red arcs appears in Baumgardner et al. [2007]. The theoretical framework for their generation is given in the review paper by Rees and Roble [1975]; their overall status within the context of magnetosphere-ionosphere coupling is summarized in Kozyra et al. [1997]. The brightness levels of SAR arcs are often less than 1000 Rayleighs (R), similar to the levels of ambient airglow arising from the natural decay of the nighttime ionosphere. Thus the low-light-level all-sky-imager (ASI) in use today records both airglow and sub-visual auroral structures simultaneously.

<sup>1</sup>Center for Space Physics, Boston University, Boston, MA, 02215, USA.

<sup>2</sup>Department of Physics and Astronomy, University of Padova, I-35122, Padova, Italy.

<sup>3</sup>Department of Electronic and Electrical Engineering, University of Bath, BA2 7AY, United Kingdom.

<sup>4</sup>Institute for Complex Systems, ISC-CNR, 50019 Sesto Fiorentino - Firenze, Italy.

<sup>5</sup>William B. Hanson Center for Space Science, University of Texas, Dallas, TX, USA.

Corresponding author: J. Wroten, Center for Space Physics, Boston University, Boston, MA 02215 USA. (jwroten@bu.edu)

[4] While auroral imaging was pioneered in Europe, most of the ASIs in use today are in North America. This has occurred for a variety of reasons. Perhaps first is the fact that the growth of cities and associated lights throughout western Europe reduced the utility of many astronomical observatories in favor of ones in more remote locations (e.g., Canary Islands, South America, Hawaii). Not only did these new locations have virtually no light pollution, but also far better statistics for clear-night weather patterns. For geophysical optical observations, the same factors ended the use of film-based or image-intensified ASIs to document airglow and sub-auroral emission features above mid-latitude Europe. Here we report on the re-introduction of all-sky optical aeronomy from a European site, and demonstrate how current CCD technologies and narrow-band interference filters can be used to capture *sub-auroral zone Space Weather* over the full continent from a single location.

## 2. Site Selection

[5] Western Europe is not only spatially less extensive (in kilometers) than North America, but it is also at higher geographic latitudes. Auroral effects are ordered by geomagnetic latitude, and at European longitudes the difference between the two latitude systems is  $\sim 5^\circ$ , with geographic being higher. Thus, a sub-auroral feature (e.g., at  $50^\circ$  N geomagnetic) occurs at a geographic latitude of  $\sim 55^\circ$  N. In North America, at longitudes where the maximum tilt of the geomagnetic dipole occurs, geomagnetic latitudes are higher than geographic by  $\sim 12^\circ$ . The same sub-auroral feature at  $50^\circ$  N magnetic would occur at the

lowest geographic latitude in the hemisphere ( $\sim 38^\circ$  N). Large networks of ASIs are therefore needed to cover the vast east–west continental extent of auroral phenomena above Canada, such as the 20 ASIs deployed for the THEMIS mission [Mende *et al.*, 2008]. In Europe, due to the combination of high geographic latitudes and converging meridians of longitude, the field-of-view (FOV) of an all-sky (“fish-eye” lens) captures sufficient “geomagnetic space” from a single location to nearly span the continent.

[6] To take advantage of these geographical/geomagnetic characteristics, we established an All-Sky-Imaging-Air-Glow-Observatory (ASIAGO) at the Cima Ekar station of the Padova Observatory ( $45.8^\circ$  N,  $11.5^\circ$  E,  $41^\circ$  magnetic, 1136 meters altitude) in northern Italy [Mendillo *et al.*, 2012]. Figure 1 shows an example of a raw data image that portrays the full  $180^\circ$  field of view. Zenith is at the center and the cardinal directions (N, S, E, W) are indicated in panel (a). There are trees and observatory domes that obstruct the FOV at some azimuths, but not to the north. One benefit of a digital image is that, since each pixel has unique elevation and azimuth angles associated with it, the data can be re-cast using those coordinates, as shown in panel (b). This is the view of the aurora low on the horizon and the SAR arc above it that one would see standing at the site and facing north---if the human eye were sensitive enough to see these normally sub-visual features.

[7] The standard way to portray all-sky data is to assign each pixel a latitude and longitude appropriate for the height of the specific emission being observed. First the spatial distortions introduced by the fish-eye lens are determined using known star locations and then the raw

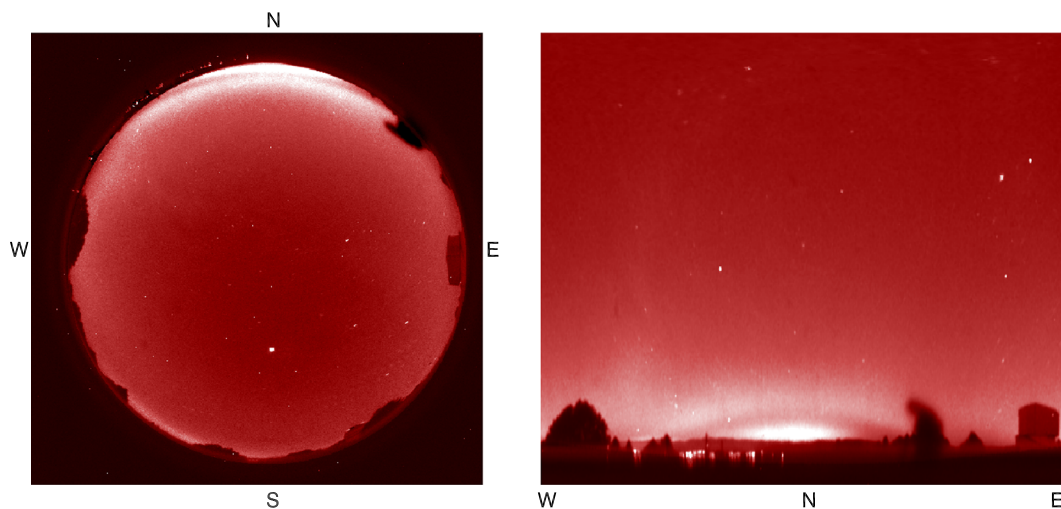


**Figure 1.** (left) An all-sky image in  $6300 \text{ \AA}$  emission taken from the Cima Ekar observatory in Asiago, Italy, on 26 September 2011, averaged using four exposures between 00:43–1:20 UT. Zenith is at the center and the cardinal directions are marked. To the north appears the diffuse aurora just above the horizon, with a stable auroral red (SAR) arc above it. Trees and observatory domes obscure low elevation angle views at some azimuths. The bright feature to the south is Jupiter. (right) The northern portion of the image displayed on an azimuth and elevation angle coordinate system (see text).

data are “unwarped” and placed upon a geographic map. Figure 2 shows how this is done for the Asiago location. There are two circular FOVs shown that relate to the two auroral morphology features that can be seen from this site using an oxygen 6300 Å (“red line”) filter. The inner circle is for the diffuse aurora at a mean height of 200 km, as typically generated by the precipitation of low energy electrons and ions from the magnetospheric plasma sheet [Semeter et al., 1999; Lummerzheim et al., 2001; Galand and Chakrabarti, 2006]. The outer circle is for SAR arc emissions (at a centroid height of 400 km) that are generated by downward heat conduction from the magnetospheric ring current along the plasmapause [Rees and Roble, 1975]. We now describe our initial detections of both diffuse aurora and a SAR arc observed from this site. We relate their locations to the F-layer’s peak electron density observed at the sub-auroral ionosonde station in Chilton (UK) shown in Figure 2.

### 3. Observations: Optical and Radio

[8] Figure 3 shows the time history of the moderate geomagnetic storm that occurred on the night of 26–27 September 2011. The Dst index shows that the main phase

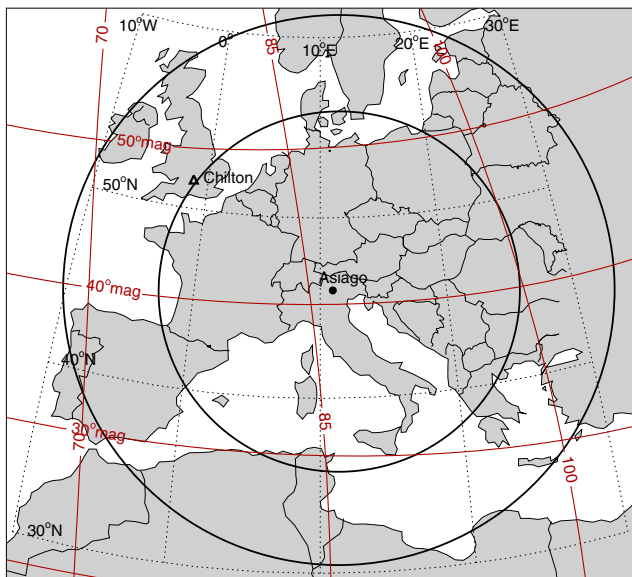


**Figure 2.** The  $\pm 85^\circ$  zenith angle field-of-view (FOV) of the ASIAGO instrument (location denoted by a solid dot) portrayed using two typical heights for 6300 Å emission caused by auroral processes. The inner circle relates to the diffuse aurora generated near 200 km altitude, while the outer circle relates to stable auroral red (SAR) arc emission generated near 400 km altitude. The dotted lines in black give geographic coordinates, while the solid lines in red give geomagnetic coordinates. The ionosonde station at Chilton (UK) is indicated by the triangle symbol.

reached its maximum disturbance of  $-103$  nT at 23:00 UT, with a typical pattern of recovery after that. The  $K_p$  indices reached their maximum values (6+) between 15:00–20:00 UT, i.e., during the 3-hour period prior when the geomagnetic field was changing most precipitously. Below the indices, times are noted when diffuse aurora and a SAR arc were observed.

[9] A selection of images showing the diffuse aurora appears in Figure 4 (left panels) using the 200 km emission height (inner circle in Figure 2). The images in the right column show the SAR Arc using the 400 km emission height (outer circle in Figure 2). The images are shown at approximately 1-hour separations in Universal Time (with  $LT = UT + 46$  minutes). The observed 6300 Å brightness levels, given in the aeronautical unit of Rayleighs (R), were calibrated as emission levels above the mean of the previous night (25 September 2011, a geomagnetically quiet night). Note that the color bar for the brightness of the diffuse aurora ranges from typical airglow levels (100s of Rayleighs) up to a maximum of  $\sim 8$  kilo-Rayleighs that approaches the threshold for visual detection at a dark location. The color bar for the SAR arc describes much lower brightness levels.

[10] With optical observations beginning after sunset, the initial image (at 18:12 UT) shows the optical remnant of sunset (and daytime ambient 6300 Å airglow) to the west; spanning the northern portion of the FOV is a clear case of diffuse aurora. The appearance of diffuse aurora is not, in itself, an unusual event. All displays of visible auroral curtains and arcs at high latitudes (called discrete aurora), distributed in an oval about the north geomagnetic pole, have regions of faint diffuse aurora equatorward of the main oval. At European longitudes, auroral oval locations are typically in northern Scandinavian countries, and thus the discrete aurora on this night are simply beyond the northern extent of ASIAGO’s FOV. Our attention here is for mid-latitude Europe and the diffuse aurora that can extend for several degrees equatorward from the main oval.

[11] The images at 19:02 and 20:04 UT are clearly post-sunset, and the 6300 Å diffuse aurora are prominent throughout this pre-midnight time sector. This indicates that the precipitation of plasma sheet charged particles is relatively constant in position—with the southern boundary of precipitation stretching from Ireland at  $\sim 10^\circ$ W longitude, across northern Germany and Poland, to Belarus at  $\sim 20^\circ$ E longitude. There is a burst of emission extending from the southern tips of Norway and Sweden down to most of Denmark ( $\sim 53^\circ$ N) captured in the image taken at 21:19 UT. Both types of precipitation, steady and sporadic, produce ionospheric plasma changes to be described in the next section. By 22:08 UT, the diffuse aurora has faded to earlier brightness levels.

[12] The more rare event captured on this night is the appearance of a SAR arc at mid-latitudes. We believe that the images in Figure 4 (right panels) represent the first all-sky, two-dimensional portrayal of a SAR arc in Europe—coming over fifty-five years after its discovery.

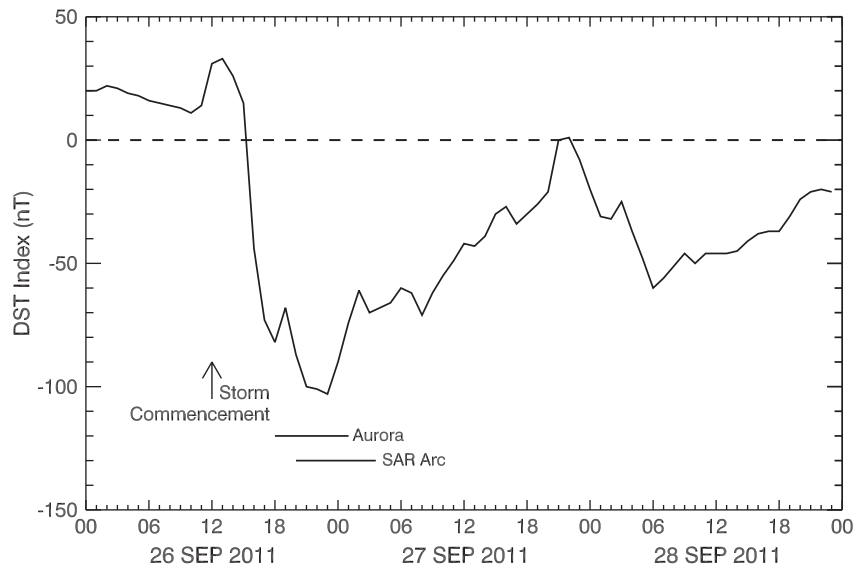


**Figure 3.** Characteristics of the geomagnetic storm of 26–28 September 2011 as portrayed using the Dst index (in nano-Tesla). Periods of observations of diffuse aurora and a SAR arc (shown in Figure 4) are indicated.

Starting with the image at 23:11 UT, it is initially difficult to see the SAR arc as an unambiguous feature distinct from the diffuse aurora. Its appearance is clear in the image at 00:06 UT (27 September). In subsequent images, from 01:08 to 03:00 UT, the classic features of stability in space and brightness appear. The last image also captures the approaching glow of sunrise in the east (right).

## 4. Space Weather Effects Associated with Diffuse Aurora

### 4.1. Peak density of the F-layer at a typical sub-auroral location

[13] The optical emissions shown in Figure 4 do not, in themselves, have an impact on technological systems. For example, they are too faint to interfere with any visible light recording systems. However, their spatial locations and time histories show unambiguously where the ionospheric F-layer’s maximum electron density ( $N_{\max}$ ) and total electron content (TEC) exhibit nighttime disturbances over vast regions. Such ionospheric storm effects are well known from long-term observations made using radio techniques [Prölss, 1995; Mendillo, 2006]. For example, Figure 5 shows observations of  $N_{\max}$  from the radio sounding (“ionosonde”) station in Chilton, England, during the night. The location of Chilton (51.6°N, 1.3°W; 47.7° magnetic latitude) is shown by the triangle symbol near London added to the map and to the images in Figures 2 and 4. The shading in Figure 5 gives the monthly mean  $\pm 1\sigma$  (standard deviation) and shows typical diurnal behavior for a mid-latitude ionospheric site.

[14] The geomagnetic storm commencement on 26 September provoked an ionospheric response as typically observed in Europe: an ionospheric storm with its initial positive phase far less dramatic than its subsequent negative phase. The transition between these phases can often be abrupt, resulting in severe ionospheric gradients in space and time. Such an event occurred during this storm, as shown by the rapid transition prior to sunset from high to low  $N_{\max}$  values—at a rate far greater than ever occurs due to normal post-sunset chemical recombination. Such an abrupt transition is the signature of the ionospheric trough and magnetospheric plasmapause location passing by the observing station [Mendillo *et al.*, 1974]. A recent review of trough characteristics and processes appears in Rodger [2008].

[15] The northern wall of the trough is caused by precipitation of low energy particles ( $\sim 100$  eV) from the magnetospheric plasma sheet. These same particles cause the diffuse aurora via excitation of oxygen in the thermosphere. When diffuse aurora appeared above the UK at 19:00 UT, the rapid decay of the ionospheric  $N_{\max}$  was interrupted by a highly irregular pattern of fluctuating electron densities. Radio communication links during such events undergo signal fluctuations (“amplitude scintillations”)—a long-studied and well-documented intrusion of auroral effects upon the mid-latitude ionosphere during geomagnetic storms [Aarons and Allen, 1971]. The equatorward edge of the diffuse aurora in the left column of Figure 4 indicates the lowest latitude where radiowave signal fluctuations will occur (the “Scintillation Boundary”) as a function of longitude and time over a vast portion of the continent.

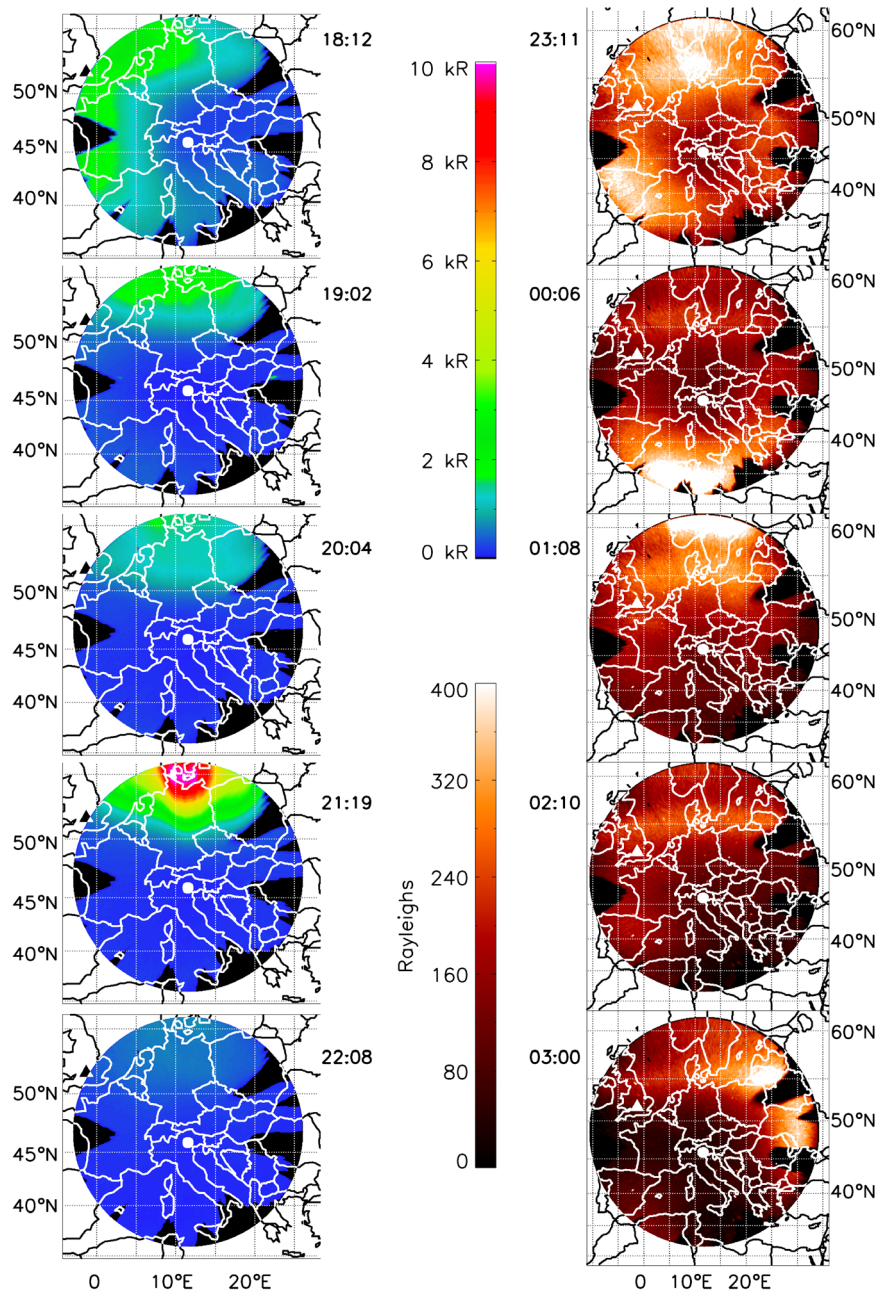


**Figure 4.** Images obtained using the ASIAGO system on the night of 26–27 September 2011. The units are in Rayleighs (R) and give the brightness levels above the mean of the previous night (25 September was geomagnetically quiet). The white dot in each image shows the location of the imager; the triangle shows the location of the Chilton ionosonde. (Left column) Examples of the diffuse aurora sampled at approximately hourly intervals during the pre-midnight period and displayed using the 200 km FOV shown in Figure 2. (Right column) Examples of the SAR arc at approximately hourly intervals in the post-midnight period and displayed using the 400 km FOV shown in Figure 2. All times are in UT and the images were obtained using a 5-minute integration time initiated at the times indicated. Trees and buildings obscure observations at some azimuths.

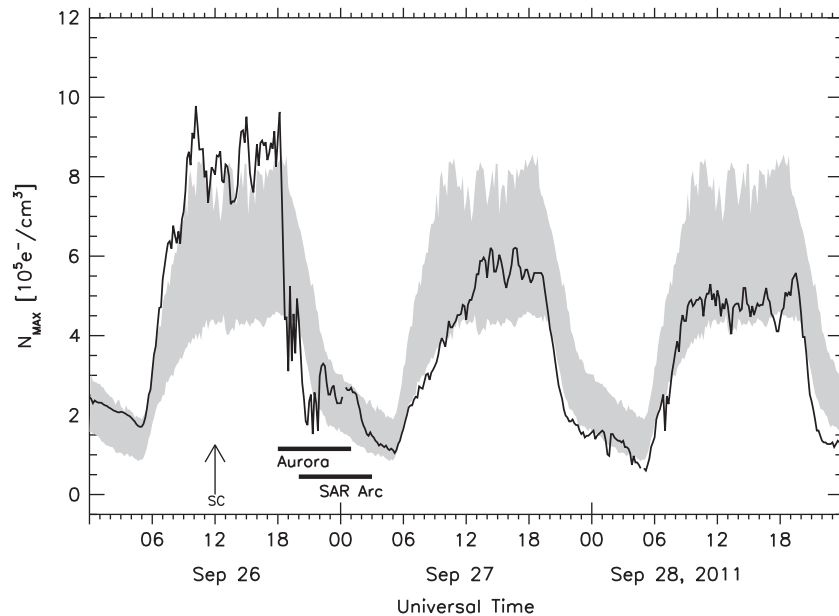


**Figure 5.** Behavior of the maximum electron density of the ionosphere ( $N_{\max}$ ) observed by the ionosonde at Chilton (UK) for 26–28 September 2011. Data are at 10-minute intervals, and the shading shows the monthly mean  $\pm 1\sigma$  (standard deviation). The geomagnetic storm that had a sudden commencement (SC) at mid-day on the 26<sup>th</sup> provoked an ionospheric storm with typical positive and negative phases (with respect to the monthly mean). During the transition from the former to the latter, a dramatic gradient occurs that is modified by irregular enhancements in  $N_{\max}$  caused by the auroral particles that excite the diffuse aurora shown in Figure 4 (left column).

#### 4.2. Maps of F-layer total electron content

[16] A second manifestation of space weather is the effect that magnetospheric particles have upon the ionosphere’s total electron content (TEC). Precise ranging for positioning using Global Navigation Satellite Systems (GPS, Galileo) relies on minimal errors introduced by the ionosphere. These include any unanticipated temporal fluctuations in signal amplitude or phase, as well as severe spatial gradients of the TEC (and therefore time delays) along trans-ionospheric ray paths. The many networks of GPS receivers now available can be used to produce regional and global maps of the ionosphere’s TEC. In Europe, one such effort is available from the website [www.bath.ac.uk/elec-eng/invert/iono/rti.html](http://www.bath.ac.uk/elec-eng/invert/iono/rti.html) maintained by the University of Bath. These maps utilize a network of approximately 70 GPS receivers for coverage of continental Europe and can yield TEC maps with a spatial resolution of  $2^\circ$  in latitude and  $4^\circ$  in longitude [Mitchell, 2002; Kinrade *et al.*, 2012, and references therein].

[17] Figure 6 shows the Bath TEC maps during the time span of optical data shown in Figure 4. The spatial coverage is  $32^\circ$ – $72^\circ$ N geographic latitude and  $24^\circ$ W– $36^\circ$ E in longitude. This exceeds the latitude extent of the optical all-sky observations ( $30^\circ$ – $60^\circ$ N) in order to show a larger context. Starting with the 18 UT map on September 26, one can see the end of the daytime positive phase

ionospheric storm, with TEC increasing towards lower latitudes. At  $\sim 60^\circ$  N, the ionospheric trough first becomes apparent (color-coded deep blue for  $\sim 5$  TEC units), and it develops further in the following panel at 19:00 UT. By 20:00 UT, the trough appears as a broad feature in latitude ( $>10^\circ$ ), with its poleward wall determined by the strong precipitation in the auroral oval (beyond the imager’s FOV). Yet, the optical images in Figure 4 (left panels) place the equatorward edge of the diffuse aurora at  $\sim 52^\circ$ N, confirmed by the effects noted in the Chilton ionosonde. As discussed above, the poleward wall of the trough is caused by precipitating plasma sheet particles—the same particles that create the equatorward edge of the diffuse aurora. Thus the trough in TEC is actually narrower than portrayed at this time, pointing out how different instrument sensitivities and spatial resolution play key roles in defining boundaries. There is clearly a synergy possible between TEC morphologies on the broadest possible scale and the finer resolution of ionospheric boundaries achieved with optical imagery, but over a less extensive FOV.

[18] A clear example of how a localized increase in precipitation can be seen in both an optical image and a TEC map occurred shortly after 21:00 UT. As shown in Figure 3, the main phase of the geomagnetic storm peaked between 21:00–23:00 UT. The optical data at 21:19 UT show a prominent bright region in northern Germany and Denmark (latitudes  $>55^\circ$ ), the brightest ( $\sim 10$  kR) period

of diffuse aurora on this night. One would expect a simultaneous enhancement in the poleward wall of the trough. In the TEC map at 21:20 UT, there is a clear enhancement from 58°–64°N, further to the north in Sweden, Norway and Finland. While this TEC enhancement occurred in the auroral oval, the lowest-energy precipitation clearly extended to lower latitudes in the classic pattern for diffuse aurora. At ~22:00 UT, from the equatorward edge of the trough to the auroral oval, the TEC map exhibits lingering low-magnitude plasma structures, while the corresponding optical image portrays a featureless pattern of minimal auroral input.

## 5. Space Weather Effects Associated with a Stable Auroral Red Arc

### 5.1. Optical images and TEC maps showing trough/plasmapause location

[19] Turning to the SAR arc event between 23:00–03:00 UT, the arc’s persistent location at 56° N falls within the vast region of low TEC values—but one with a clear trough at 56°N in the TEC maps. SAR arcs can be as narrow as 1° in latitude (~100 km at F-layer heights), as shown in the event studied by *Foster et al.* [1994]. The 2° latitude resolution of the TEC maps was clearly successful in locating the trough at its narrowest latitude width of the night (at 00:10 and 01:10 UT). This coherence of SAR arc and trough locations is an impressive first use of all-sky-images and GPS TEC maps to show where heat conduction from the ring current/plasmapause location reaches the ionosphere in latitude, longitude and local time.

### 5.2. In-situ satellite observations of SAR arc parameters

[20] Complementary views of ionospheric latitude structures on this night can be obtained from *in-situ* data from the DMSP-15 satellite that passed through the ASIAGO FOV at the end of the optical observing period. Figure 7 depicts plasma parameters measured at ~840 km during the pass that occurred over this region between 03:50–03:59 UT—about an hour after the last image shown in Figure 4. The narrow nature of the trough in ion density ( $N_i$ ) is seen, together with the high electron temperatures ( $T_e$ ) that occur at the plasmapause location along the equatorward edge of the trough. This topside ionosphere view of the trough is consistent with known trough morphologies as a function of height [*Mendillo and Chacko, 1977*]. The peak in electron temperature shows unambiguously that the SAR arc has moved to a lower geographic latitude (52.5°N) than the SAR arc location (~56°N) shown in the post-midnight images in Figure 4. This is consistent with plasmapause contraction from midnight to dawn. A subsequent DMSP pass nearly two hours later (right panel in Figure 7) shows the persistence of these features under sunlit conditions. Solar production effects have caused the trough’s equatorward edge to have less of a gradient. Higher plasma densities cool the electron gas and thus the  $T_e$  peak magnitude is about 1000 degrees lower than

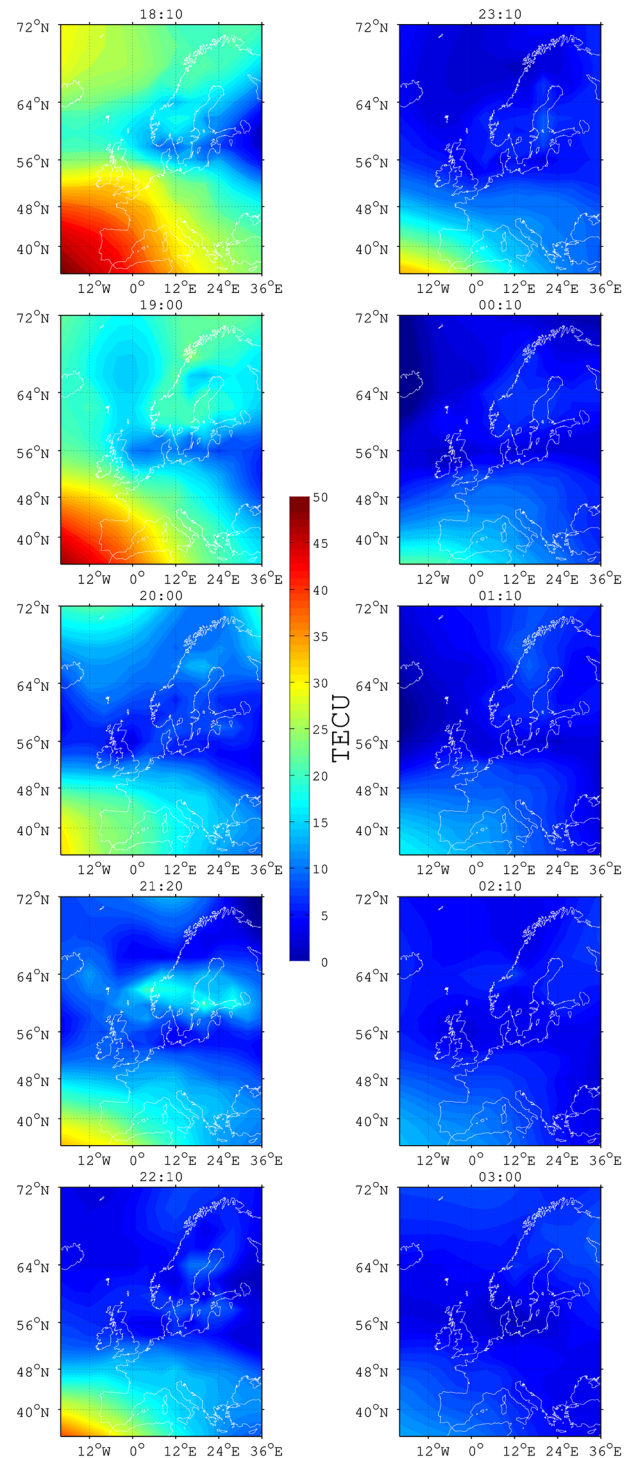


**Figure 6.** Maps of total electron content (TEC) for the night of 26–27 September 2011, obtained using a network of ~70 GPS receivers in Europe. TEC units are in  $10^{12} \text{ e}^-/\text{cm}^2$ . The TEC data are shown at UT times (in hours and minutes), with the left and right columns corresponding approximately to the times of the optical images shown in Figure 4. Spatial resolution of the TEC maps is 2° in latitude and 4° in longitude.

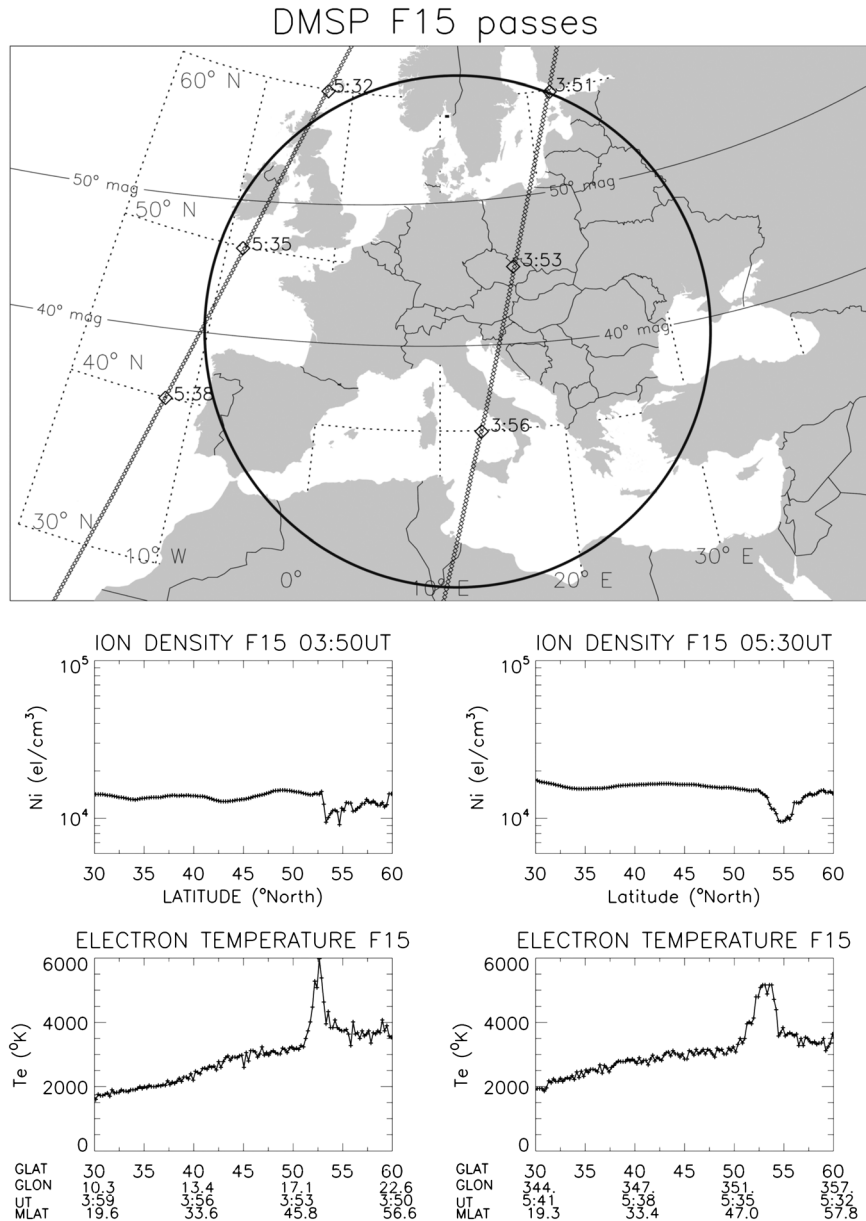


**Figure 7.** Plasma observations from the Defense Meteorological Satellite Program (DMSP) shown in relation to the FOV of the ASIAGO instrument. Two passes of the F15 satellite at 840 km are shown: the first at 03:50 UT (~1 hour after the last image showing the SAR arc) that samples a major portion of the all-sky FOV, and a second at 05:30 UT to the west of the FOV (after local sunrise). In the lower panels, the total ion density ( $N_i$ ) and electron temperatures ( $T_e$ ) measured at 840 Km are shown. In the left panel, the location of the plasmopause is clearly defined in latitude by the  $N_i$  gradient at 53°N. The  $T_e$  peak of 5980°K occurs at the same latitude—defining the location of the SAR arc. The same effects are seen in the subsequent satellite pass. The widths of the SAR arcs correspond roughly to the latitude regions with  $T_e$  4000° K at DMSP’s height [Baumgardner et al., 2007].

found on the previous (nighttime) pass. The  $T_e$  values above 4000°K can still be associated with the SAR arc—indicating that it would be fainter and broader in north-south extent.

## 6. Impacts and Assessments

[21] Radiowave scintillations occur due to the small-scale plasma irregularities produced by any form of auroral

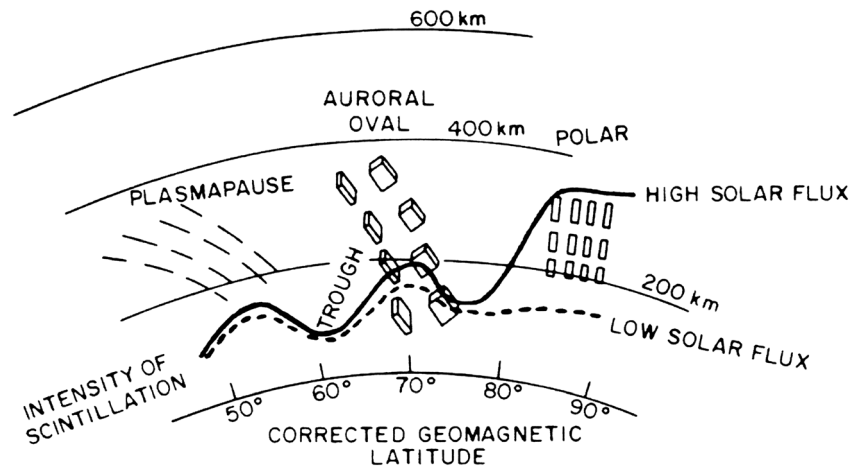


**Figure 8.** The two components of sub-auroral scintillations activity, as depicted in *Aarons* [1982, 1987]. The lowest latitude scintillations are associated with the plasmopause (near the equatorward edge of the trough minimum); the higher latitude zone is associated with the inner edge of the plasmasheet (poleward of the trough minimum). The solid lines give a representation of scintillation strength at solar maximum, and the dashed lines at solar minimum. At polar cap latitudes (extreme right), strong scintillations are present only during solar maximum years. While this schematic implies a nighttime latitude profile at a fixed longitude and local time, the images in Figure 4 show that the sub-auroral boundaries can be specified over a broad range of spatial and temporal conditions using all-sky 6300 Å imagery.

precipitation. During geomagnetic storms, these ionospheric irregularities move from auroral to sub-auroral latitudes. Pioneering studies of such effects introduced the concept of a “Scintillation Boundary” that simply shifted equatorward by amounts dependent upon the severity of the geomagnetic activity [Aarons and Allen, 1971; Aarons, 1982]. The concept of a single boundary—with plasmasheet precipitation-induced irregularities in the F-layer co-located with the poleward wall of the trough—was later replaced by a double boundary. The second, distinct zone of radiowave amplitude scintillations was associated with the plasmopause/SAR arc zone of irregularities equatorward of the trough’s minimum. This SAR arc component is discussed in Aarons [1987, and references therein], and summarized in Figure 8. The specific cause of the lower-latitude irregularity zone is an active field of research. Irregularities produced by sub-auroral polarization streams (SAPS) within the trough, or irregularities associated with low-energy precipitation within the SAR arc itself, are options under study. The current picture, then, is that scintillations occur within regions to either side of the trough’s minimum. The images in Figure 4 show where both boundaries occur spanning the continent on the night of 26–27 September 2011. Our check of the GPS phase fluctuations along the raypaths used to make the TEC maps revealed a clear scintillation boundary at  $\sim 58^\circ\text{N}$ —precisely where the equatorward edge of the diffuse aurora appeared. The high frequencies (UHF) used for GPS did not record scintillations associated with the SAR arc—an effect more associated with the use of lower (VHF) frequencies.

[22] The results presented here for a single disturbed period offer an opportunity to explore and to validate how space weather effects over mid-latitude Europe can be predicted with the aid of wide-angle, low-light-level optical techniques. Current forecasting and now-casting methods for geomagnetic storm effects over Europe utilize observations clustered around auroral and polar cap latitudes. For example, the recent study by Machol *et al.* [2012] dealt with the possibility of predicting visible auroral displays, and thus only for geomagnetic latitudes above  $50^\circ\text{N}$  at European longitudes. Here we have treated the lower energy aspects of storm-time auroral input, showing that sub-visual emissions point to disturbances in the F-layer’s peak electron density and integrated electron content that extend further south.

[23] Forecasting techniques using ionosondes in Europe are the basis of the Digital upper Atmosphere Server (DIAS) described by Belehaki *et al.* [2006]. DIAS uses the ionosondes at Chilton and seven others to provide low resolution maps of F-layer conditions relevant to communications and navigation needs. Post-event validation between 6300 Å images and DIAS maps (or other near real-time forecasts) for this 26–27 September 2011 event are beyond the scope of this paper, but clearly are possible. Follow-up investigations should focus on how new optical data sets from one or more sites that reveal structures and boundaries at high spatial resolution can best be utilized. For example, the climatological scintillation model of Wernik *et al.* [2007] deals successfully with past observations of scintillation intensity versus time of day and season for the high latitude ionosphere in the Northern Hemisphere. Its extension to

the mid-latitude, sub-auroral domain could be validated by data such as shown here. Given that optical data can only be obtained during nighttime hours, and only on clear nights, while DIAS and GPS- (or Galileo-) based TEC maps can be made under all conditions, all-sky imaging is less available for routine now-casting uses. Its role would be more meaningful in retrospective evaluations of model predictions for space weather events spanning mid-latitude Europe.

[24] **Acknowledgments.** This work was supported initially by seed research funds for testing new instrumentation provided through the Center for Space Physics at Boston University. Subsequent data analysis and an instrumentation upgrade were made possible by a grant from the Aeronomy Program at NSF (J. B., P I). Analysis funds were provided from the Office of Naval Research (for M.M. and J.W.) and NSF and NASA (for C.M.). We thank Ms. Clara Narvaez for her assistance in the analysis of ionosonde data.

## References

- Aarons, J. (1982), Global morphology of ionospheric scintillations, *Proc. IEEE*, *70*, 360–378.
- Aarons, J. (1987), F layer irregularity observations of the SAR arc event of March 5–6, 1981, *Radio Sci.*, *22*, 100–110.
- Aarons, J., and R. S. Allen (1971), Scintillation boundary during quiet and disturbed magnetic conditions, *J. Geophys. Res.*, *76*, 170–177.
- Akasofu, S.-i. (1968), *Polar and Magnetospheric Substorms*, Springer-Verlag, New York.
- Barbier, D. (1958), L'activite aurorale aux bass latitudes, *Ann. Geophys.*, *14*, 334–355.
- Barbier, D. (1960), L'arc auroral stable, *Ann. Geophys.*, *16*, 544–549.
- Baumgardner, J., J. Wroten, J. Semeter, J. Kozyra, M. Buonsanto, P. Erickson, and M. Mendillo (2007), A very bright SAR arc: implications for extreme magnetosphere-ionosphere coupling, *Ann. Geophys.*, *25*, 2593–2608.
- Behlke, A., L. Cander, B. Zolesi, J. Bremer, C. Juren, I. Stanislawska, D. Dialektis, and M. Matzopoulos (2006), Monitoring and forecasting the ionosphere over Europe: The DIAS Project, *Space Weather*, *4*, S12002, doi:10.1029/2006SW000270.
- Eather, R. H. (1980), *Majestic Lights: The Aurora in Science, History and the Arts*, AGU, Washington, DC.
- Foster, J. C., M. J. Buonsanto, M. Mendillo, D. Nottingham, R. J. Rich, and W. Denig (1994), Coordinated stable auroral red arc observations: Relationship to plasma convection, *J. Geophys. Res.*, *99*, 11,429–11,439.
- Galand, M., and S. Chakrabarti (2006), Proton aurora observed from the ground, *J. Atmosph. Solar-Terr. Phys.*, *68*, 1488–1501.
- Kinrade, J., C. N. Mitchell, P. Yin, N. Smith, M. J. Jarvis, D. J. Maxfield, M. C. Rose, G. S. Bust, and A. T. Weatherwax (2012), Ionospheric scintillation over Antarctica during the storm of 5–6 April 2010, *J. Geophys. Res.*, *117*, A05304, doi:10.1029/2011JA017073.
- Kozyra, J. U., A. F. Nagy, and D. W. Slater (1997), High-altitude energy source(s) for stable auroral red arcs, *Rev. Geophys.*, *35*, 155–190.
- Lummerzheim, D., M. Galand, J. Semeter, M. J. Mendillo, M. H. Rees, and F. J. Rich (2001), Emission of OI(630 nm) in proton aurora, *J. Geophys. Res.*, *106*, 141–148.
- Marchol, J. L. et al. (2012), Evaluation of OVATION Prime as a forecast model for visible aurorae, *Space Weather*, *10*, S03005, doi:10.1029/2011SW000746.
- Mende, S., S. Harris, H. Frey, V. Angelopoulos, C. Russell, E. Donovan, B. Jackel, M. Greffen, and L. Peticolas (2008), The THEMIS array of ground-based observatories for the study of auroral substorms, *Space Sci. Rev.*, *141*, 357–387, doi:10.1007/s11214-0089380-x.
- Mendillo, M. (2006), Storms in the ionosphere: Patterns and processes for total electron content, *Rev. Geophys.*, *47*, RG4001.
- Mendillo, M., C. Barbieri, J. Baumgardner, J. Wroten, G. Cremonese, and G. Umbriaco (2012), A stable auroral red arc over Europe, *Astron. Geophys.*, *53*(1), 16–18.
- Mendillo, M., and C. C. Chacko (1977), The baseline ionospheric trough, *J. Geophys. Res.*, *82*, 5129–5137.
- Mendillo, M., J. Baumgardner, J. Aarons, J. Foster, and J. Klobuchar (1987), Coordinated optical and radio studies of ionospheric disturbances: Initial results from Millstone Hill, *Annales. Geophysicae*, *5A*(6), 543–550.
- Mendillo, M., J. Klobuchar, and H. Hajeb-Hosseini (1974), Ionospheric disturbances: Evidence for the contraction of the plasmasphere during severe geomagnetic storms, *Planet. Space Sci.*, *22*, 223–236.
- Mitchell, C. N. (2002), Imaging of near-Earth space plasma, *Philos. Trans. R. Soc. London, Ser. A*, *360*, 2805–2818.
- Pröls, G. (1995), Ionospheric F-region storms, in *Handbook of Atmospheric Electrodynamics*, vol. 2, edited by H. Volland, Chap. 8, pp. 195–248, CRC Press, Boca Raton, FL.
- Rees, M. H., and R. G. Roble (1975), Observations and theory of the formation of stable auroral red arcs, *Rev. Geophysics and Space Phys.*, *13*, 201–242.
- Rodger, A. (2008), The mid-latitude trough—Revisited, in *Midlatitude Ionospheric Dynamics and Disturbances*, edited by Kintner, et al., AGU, Geophysical Monograph #181, Washington, DC.
- Semeter, J., M. Mendillo, and J. Baumgardner (1999), Multispectral tomographic imaging of the midlatitude aurora, *J. Geophys. Res.*, *104*, 24,565–24,585.
- Weber, E., and J. Buchau (1981), Polar cap F-layer auroras, *Geophys. Res. Lett.*, *8*, 125–128.
- Weber, E., J. Buchau, J. Moore, J. Sharber, R. Livingston, J. Winningham, and B. Reinisch (1984), F-layer ionization patches in the polar cap, *J. Geophys. Res.*, *89*, 1683–1694.
- Wernik, A., L. Alfonsi, and M. Materassi (2007), Scintillation modeling using in situ data, *Radio Sci.*, *42*, RS1002, doi:10.1029/2006RS003512.